GA-A15558
UC-77

THE EFFECT OF AGING AND COLD WORKING ON THE HIGH-TEMPERATURE LOW-CYCLE FATIGUE BEHAVIOR OF ALLOY 800H: PART II CONTINUOUS CYCLIC LOADING

by
R. E. VILLAGRANA, J. L. KAAE, and J. R. ELLIS

Prepared under
Contract DE-AT03-76ET35300
for the San Francisco Operations Office
Department of Energy

OCTOBER 1979

GENERAL ATOMIC COMPANY

DISCLAIMER

Printed in the United States of America
Available from
National Technical Information Service
U.S. Department of Commerce
5285 Port Royal Road
Springfield, Virginia 22161
Price: Printed Copy $4.50; Microfiche $3.00

GA-A15558
UC-77

MASTER

THE EFFECT OF AGING AND COLD WORKING ON THE HIGH-TEMPERATURE LOW-CYCLE FATIGUE BEHAVIOR OF ALLOY 800H: PART II CONTINUOUS CYCLIC LOADING

by

R. E. VILLAGRANA, J. L. KAAE, and J. R. ELLIS*

Prepared under
Contract DE-AT03-76ET35300
for the San Francisco Operations Office
Department of Energy

*Oak Ridge National Laboratory, Oak Ridge, Tennessee

GENERAL ATOMIC PROJECT 6400
OCTOBER 1979

GENERAL ATOMIC COMPANY

THIS PAGE

WAS INTENTIONALLY

LEFT BLANK

ABSTRACT

The individual and combined effects of cold working (5 and 10 pct) and aging (4000 and 8000 h in the temperature range 538 to 760°C) on the high-temperature low-cycle fatigue behavior of alloy 800H have been investigated. The specimens were tested at the aging temperatures. Both the saturation stress range and the fatigue life were found to be history dependent. A history-independent hardening mechanism, dynamic strain aging, was found to operate over the temperature range ∿450 to 650°C and to be maximized at ∿550°C. It is speculated that carbon is responsible for this dynamic strain aging. Finally, at temperatures above 538°C the Coffin-Manson plots indicate the possible existence of a history-independent softening mechanism.

THIS PAGE

WAS INTENTIONALLY

LEFT BLANK

CONTENTS

FIGURES

FIGURES (continued)

TABLES

I. INTRODUCTION

This paper reports the second part of a study of the effects of aging and cold working on the low-cycle fatigue (LCF) behavior of alloy 800H in the temperature range 538 to 760°C. In the first paper, which hereafter is referred to as Part I, the effects of aging and cold working on the yield strength of alloy 800H, as determined during the first cycle of the LCF tests, were reported. In this paper the LCF tests are followed to completion, and, as in Part I, the structure of the alloy is correlated with its mechanical behavior. The engineering design data resulting from this work will be discussed in a subsequent report.

II. SYNOPSIS OF PART I

The specimens that were LCF tested were obtained from the as-received (solution-annealed) material and from material that had undergone the following treatments: aging for 4000 h and 8000 h at temperatures of 538, 593, 649, 704, and 760°C; cold working 5 and 10 pct in tension at ambient temperature; and cold working followed by thermal aging. The solution-annealed and the cold-worked specimens were fatigue tested at the various aging temperatures, while the aged specimens were tested only at their aging temperature.

The first stage of Part I was to determine the microstructure of the specimens after the various aging and deformation treatments. The phase identifications were accomplished by X-ray diffraction analysis of electrolytic extractions, while their morphologies were determined using transmission electron microscopy (TEM) and diffraction. In all, six phases were identified by X-ray diffraction: $Cr_{23}C_6$, (M,Ti)C, Ti(C,N),

TiN, a γ' phase that is a Perovskite-type carbide of the form $Ni_3(Al,Ti)C_x$, and an unknown phase which was neither the G ($Ni_{16}Si_7Ti_6$) phase nor the σ (FeCr) phase.

The results of the X-ray diffraction analysis of the carbide phases are given in Table I. Transmission electron microscopy revealed that the $Cr_{23}C_6$ was almost always located at grain boundaries, while the MC-type carbides appeared every so often as large block-like precipitates within the grains.

The γ' observations are summarized in Table II. This table has been revised to reflect new results obtained in the present study (see Section 4.1.2).

The 0.2 pct offset yield strengths that were measured during the first cycle of fatigue tests are given in Table III. It can be seen that the yield strength of the specimens decreased slightly with increasing testing temperature. Besides the usual thermal softening mechanisms, the softening that occurred above 593°C could be partly due to an increase in the mobility of interstitial carbon. (Dynamic strain aging due to carbon is discussed in Section 4.2.2).

The effect of cold working was to harden the alloy by the introduction of forest dislocations. The discrepancies seen in several of the cold-worked entries in Table III are within the realm of experimental error and are therefore not felt to be significant.

The strong increases in the yield strength that occurred during aging of specimens that had not been cold worked coincided with the formation of $Cr_{23}C_6$ at the grain boundaries. For example, substantial hardening occurred after aging at 538°C where only grain-boundary carbides were found. The maximum hardening occurred at 593°C where a large volume of $Cr_{23}C_6$

Table I. Results of X-Ray Phase Analysis of Carbide Extractions (in mg of Precipitate per 10.0 g of Alloy) (Ref. 1)

Specimen	$M_{23}C_6$	(M,Ti)C	Ti(C,N)	TiN	X
Solution annealed	1.1	10	5	3	0
5 pct c.w.*	0.9	9	6	4	0
10 pct c.w.	0.9	8	5	3	0
4000 h at 538°C	11	16	9	3	0
5 pct c.w.; 4000 h at 538°C	32	13	8	6	0
10 pct c.w.; 4000 h at 538°C	31	14	10	5	0
8000 h at 538°C	28	11	6	2	0
4000 h at 593°C	50	10	6	2	0
5 pct c.w.; 4000 h at 593°C	59	13	6	4	0
10 pct c.w.; 4000 h at 593°C	58	9	9	4	0
4000 h at 649°C	52	7	6	3	0
5 pct c.w.; 4000 h at 649°C	50	12	11	3	0
10 pct c.w.; 4000 h at 649°C	49	10	7	4	0
8000 h at 649°C	61	12	8	6	0
4000 h at 704°C	47	16	8	2	7
5 pct c.w.; 4000 h at 704°C	44	18	8	3	7
10 pct c.w.; 4000 h at 704°C	40	16	7	3	6
4000 h at 760°C	18	14	6	3	4
5 pct c.w.; 4000 h at 760°C	21	17	11	2	5
10 pct c.w.; 4000 h at 760°C	25	19	8	2	6
8000 h at 760°C	30	27	10	4	4

*c.w. = cold worked.

Table II. Revised Summary of X-Ray Diffraction and Transmission Electron Microscopy Observations of γ' Precipitation

Specimen	γ'
Solution annealed	0
5 pct c.w.	0
10 pct c.w.	0
4000 h at 538°C	0
5 pct c.w.; 4000 h at 538°C	0
10 pct c.w.; 4000 h at 538°C	0
8000 h at 538°C	0
4000 h at 593°C	0
5 pct c.w.; 4000 h at 593°C	0
10 pct c.w.; 4000 h at 593°C	0
4000 h at 649°C	Present
5 pct c.w.; 4000 h at 649°C	Present
10 pct c.w.; 4000 h at 649°C	Present
8000 h at 649°C	Present
4000 h at 704°C	Present
5 pct c.w.; 4000 h at 704°C	Present
10 pct c.w.; 4000 h at 704°C	Present
4000 h at 760°C	0
5 pct c.w.; 4000 h at 760°C	0
10 pct c.w.; 4000 h at 760°C	0
8000 h at 760°C	0

Table III. Revised Summary of 0.2 Pct Offset Yield Strengths (in MPa)*

Specimen	Aging and Testing Temperature, °C				
	538	593	649	704	760
Solution annealed	131	124	124	124	110
5 pct c.w.	276	248	234	220	227
10 pct c.w.	331	303	310	296	276
Aged 4000 h	214	282	220†	145†	124
Aged 8000 h	227	---	276†	---	124
5 pct c.w.; aged 4000 h	317	393	262†	207†	193
10 pct c.w.; aged 4000 h	420	462	324†	276†	234

*The entries marked with a dagger correspond to specimens which showed γ' formation.

and the greatest number of precipitate particles were observed, while only slight hardening occurred at 760°C where the carbide volume was low and the particles were larger in size and fewer in number. These dispersions of grain-boundary precipitates presumably harden the material by inhibiting the transfer of deformation from grain to grain.

The precipitation of γ' in the matrix did not cause as large an increase in the yield stress as the precipitation of $Cr_{23}C_6$ at the grain boundaries. Typically, the formation of $Cr_{23}C_6$ precipitates at the grain boundaries added approximately 100 MPa to the yield strength, while the formation of γ' in the matrix added less than 50 MPa to the yield strength.

The large blocky matrix carbides of the (M,Ti)C, Ti(C,N), and TiN types, which were not significantly affected by aging, were judged to have an insignificant effect on the yield strength since they would not be effective barriers to dislocation motion, although they could act as ancillary sources of dislocations.

III. EXPERIMENTAL PROCEDURE

The vendor's certified analysis of the heat of alloy 800H used in this work is given in Table IV. For brevity, experimental procedures used in this study are only minimally reported; a more detailed account is given in Part I.

Hourglass-shaped LCF specimens were machined from the solution-annealed material and from material that had undergone the aging, cold-working, and combined cold-working and aging treatments described in Section II. Fatigue testing was carried out in servo-controlled hydraulic machines with diametral strain measured at the minimum specimen diameter. The diametral strain was continuously converted to axial strain in an analog computer so that the tests could be carried out with the axial strain controlled.

Table IV. Vendor's Certified Analysis of Alloy 800H Heat Number HH5556A

Element	Wt Pct	Element	Wt Pct
Fe	44.0	Cu	0.52
Ni	33.0	Ti	0.42
Cr	20.3	Al	0.39
Mn	0.90	C	0.07

The specimens were continously cycled between equal magnitudes of tensile and compressive axial strain at a strain rate of 4×10^{-3} s^{-1}. The testing temperatures and the various mechanical and thermal treatments the specimens were given were described in Section II.

IV. RESULTS AND DISCUSSION

4.1. Microstructure

4.1.1. Carbide and Nitride Phases. When analyzing LCF experiments care must be taken to ensure that the effects of possible structural modifications induced during the tests are included. To this end, thin discs were removed from the failed regions of the specimens after completion of the LCF test. These discs were used to prepare TEM specimens and for electrolytically extracting the carbide and nitride phases for X-ray analysis.

The TEM studies of the failed regions revealed that the carbide morphologies were essentially similar to those described in Part I with $Cr_{23}C_6$ primarily confined to grain boundaries. However, vacancies are a by-product of deformation, so it is not unreasonable to assume that an increase in the diffusion rates of the elements in solid solution would occur during LCF testing. This, of course, could result in some acceleration of carbide or nitride precipitation during testing.

In order to determine quantitatively if the LCF deformation enhanced carbide precipitation, electrolytic extractions were performed on a series of solution-annealed LCF specimens and also on a series of solution-annealed specimens that were exposed to the same thermal history as the fatigue specimens, but without the concurrent deformation. The amounts of carbide and nitride phases found in the fatigue specimens, as well as the difference between the amounts of carbide and nitride phases in the LCF specimens and the control specimens, are listed in Table V. These results demonstrate

Table V. Summary of the Amounts of Carbide and Nitride Precipitation Formed During LCF Testing (in mg of Precipitate per 10.0 g of Alloy)

Temp. of Test, °C	Time at Temp., h	Strain Range, %	Difference in Amounts Between Fatigue Specimens and Similarly Aged Specimens				Amounts in Fatigue Specimens			
			$\Delta Cr_{23}C_6$	Δ(M,Ti)C	ΔTi(C,N)	ΔTiN	$Cr_{23}C_6$	(M,Ti)C	Ti(C,N)	TiN
538	4.1	2	0	1	0	-1	1	8	5	1
538	7.9	1	0	-1	-2	-1	2	7	3	2
538	31.1	0.6	7	13	8	3	10	21	14	6
593	2.9	2	1	3	1	-1	3	11	6	2
593	5.0	1	2	5	2	0	4	11	6	2
593	122	0.5	26	11	13	0	32	19	18	6
649	3.2	2	5	5	-1	0	9	13	7	3
649	4.1	1	2	1	-1	0	6	9	6	3
649	7.1	0.6	11	1	5	2	18	10	11	5
760	2.9	2	4	2	1	-2	24	10	10	1
760	3.5	1	7	1	3	1	25	11	15	3
760	6.5	0.5	-2	-1	6	0	20	9	18	3

the expected enhancement of precipitation during LCF testing, although the effect does not occur equally for all phases. For example, there was no significant change in the nitride phase, TiN, indicating that most of the available nitrogen precipitated during the melting and subsequent solution annealing of the alloy. (This observation is consistent with Part I, where the amount of TiN formed did not change significantly during aging at any of the temperatures for times up to 8000 h.)

For temperatures in the range 538 to 649°C, the amount of carbide precipitation is strongly dependent on the time at temperature; consequently, the greatest amount of precipitation occurs in the lower-strain-range tests. Comparison of the results given in Tables V and I reveals that a significant fraction of the amount of carbides found in the long-aged specimens was formed in the solution-annealed specimens tested at low strain ranges. Indeed, at all strain ranges of the 760°C tests the carbide precipitation reactions are essentially complete. Transmission electron microscopy of these specimens showed that some $Cr_{23}C_6$ precipitation could have occurred on dislocations (see Fig. 1).

4.1.2. Gamma-Prime Phase. In Part I there were several discrepancies between the X-ray and TEM observations of the γ' phase. For instance, an X-ray line-width analysis indicated that after 4000 h aging at both 649 and 704°C, γ' had nucleated and grown to approximately 1000 Å in diameter, while the TEM showed no γ' at all. Compounding these discrepancies was the observation that after 8000 h aging at 649°C, the transformation was in an early stage (see Fig. 4 of Part I) with the size of the γ' precipitates being less than 100 Å in diameter. In Part I it was suggested that large γ' precipitates could have formed at the grain boundaries and become lost, to the TEM, among the $Cr_{23}C_6$ precipitates.

In order to resolve these discrepancies, further studies were initiated following the completion of Part I. Using a scanning electron microscope equipped with an EDAX ECON detector, it was discovered

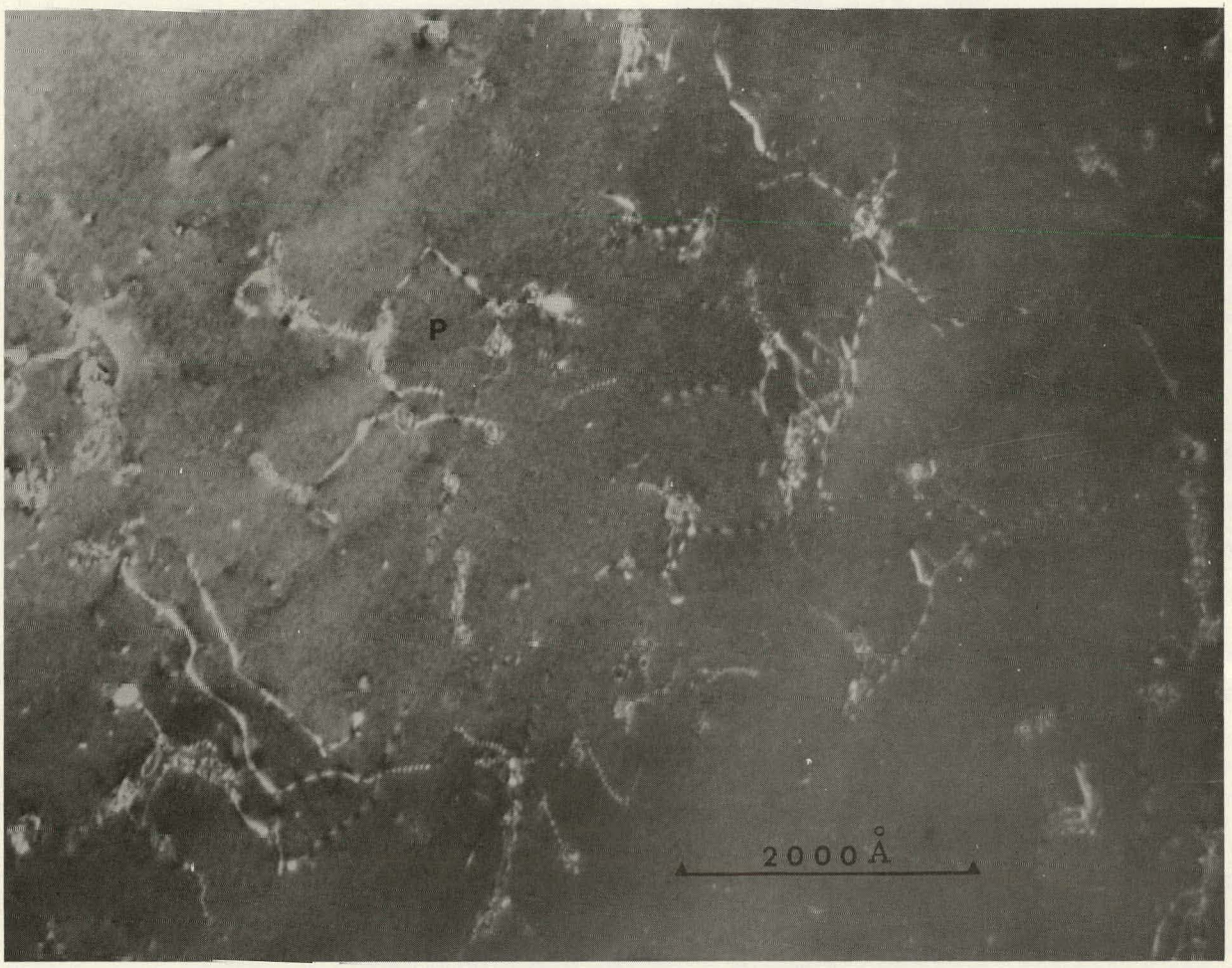

Fig. 1 - Weak-beam image from a solution-annealed specimen, tested at ε_r = 0.5 pct and 760°C, showing possible $Cr_{23}C_6$ precipitation at P. The foil was tilted away from (110) to reveal the $\bar{2}\bar{2}0$ systematics and the image was formed with $-\vec{g}$ while $2\vec{g}$ was at the Bragg condition.

that the Al and Ti content varied from grain to grain in the LCF specimens. Because there are excesses of Ni and C relative to the Al and Ti available for the γ' reaction, the rate of the reaction is expected to be sensitive to fluctuations in the Al and Ti concentrations. Little can be said beyond this, except that according to the theory of absolute reaction rates, the rate of the γ' reaction will be proportional to the product of the reactant concentrations and the specific reaction rate constant. However, it is not known how variations in the Al and Ti concentrations affect this latter term.

The X-ray analyzer was also used to determine Al and Ti concentrations in several TEM specimens taken from material aged at 649 and 704°C so that these concentrations could be compared with the observed stage of the transformation. A strong dependence was found. For example, a TEM specimen taken from a LCF specimen that was aged for 4000 h at 649°C and exhibited large γ' precipitates (similar to those shown in Fig. 5 of Part I) contained 0.294 wt pct Al and 0.508 wt pct Ti, while a specimen that was aged for 8000 h at 649°C and showed only a very early stage of γ' formation (see Fig. 4 of Part I) contained 0.271 wt pct Al and 0.303 wt pct Ti. Thus, the inconsistencies in the X-ray and TEM observations can be attributed to differences in γ' formation due to differences in the Al and Ti concentrations.

Low-cycle fatigure testing is expected to accelerate the γ' precipitation reaction through enhanced diffusion, just as it does for the carbide precipitation reactions. However, because of the nonuniformity of γ' formation throughout the specimens, experimental confirmation of this was not possible.

No γ' precipitation was observed in TEM specimens taken from the non-aged specimens tested at 649 and 704°C.

4.1.3. Defect Structure. In a recent review paper Orr[2] has put forth an argument favoring γ' formation as the principal hardening mechanism for alloy 800. Orr argues that in specimens where TEM does not reveal γ' formation, the hardening is caused by a short-range ordering reaction that is a precursor to the γ' transformation. As evidence for this theory, Orr presents bright field TEM pictures of "super-dislocations," without selected area diffraction patterns and without stating the diffraction conditions. Since these TEM data are unacceptable in identifying short-range ordering (double dislocation images in a bright field can arise when more than one Bragg maximum is strongly excited), both weak-beam imaging and an analysis of the diffuse scattering in selected area diffraction patterns were employed in looking for evidence of short-range ordering. After LCF testing, the solution-annealed specimens that were tested at 649 and 704°C were examined for short-range ordering; none was found. As additional proof, Thompson[3] has conducted neutron diffraction studies on an alloy of 800H containing 0.39 wt pct Al and 0.44 wt pct Ti and finds no evidence of ordering after aging 1000 h at 649°C.

The dislocations that form in the alloy are predominately extended; this would explain the effectiveness of $Cr_{23}C_6$ precipitation at the grain boundaries in hardening the material (Fig. 2). However, after LCF testing, pure planar arrays of dislocations were not unique to every grain since some cross slip had occurred. At the highest testing temperatures there was a tendency to form subgrain boundaries during the LCF test (Fig. 3); the number density of these boundaries seemed to increase both with temperature and with the length of the test.

Kestenbach[4] has studied the effect of applied stress on the separation of partial dislocations and dislocation substructure in a commercial 304 stainless steel and concludes that the separation of the Shockley partials, and hence the amount of cross slip that occurs in austenitic stainless steels, is a function of the orientation of a particular grain with respect

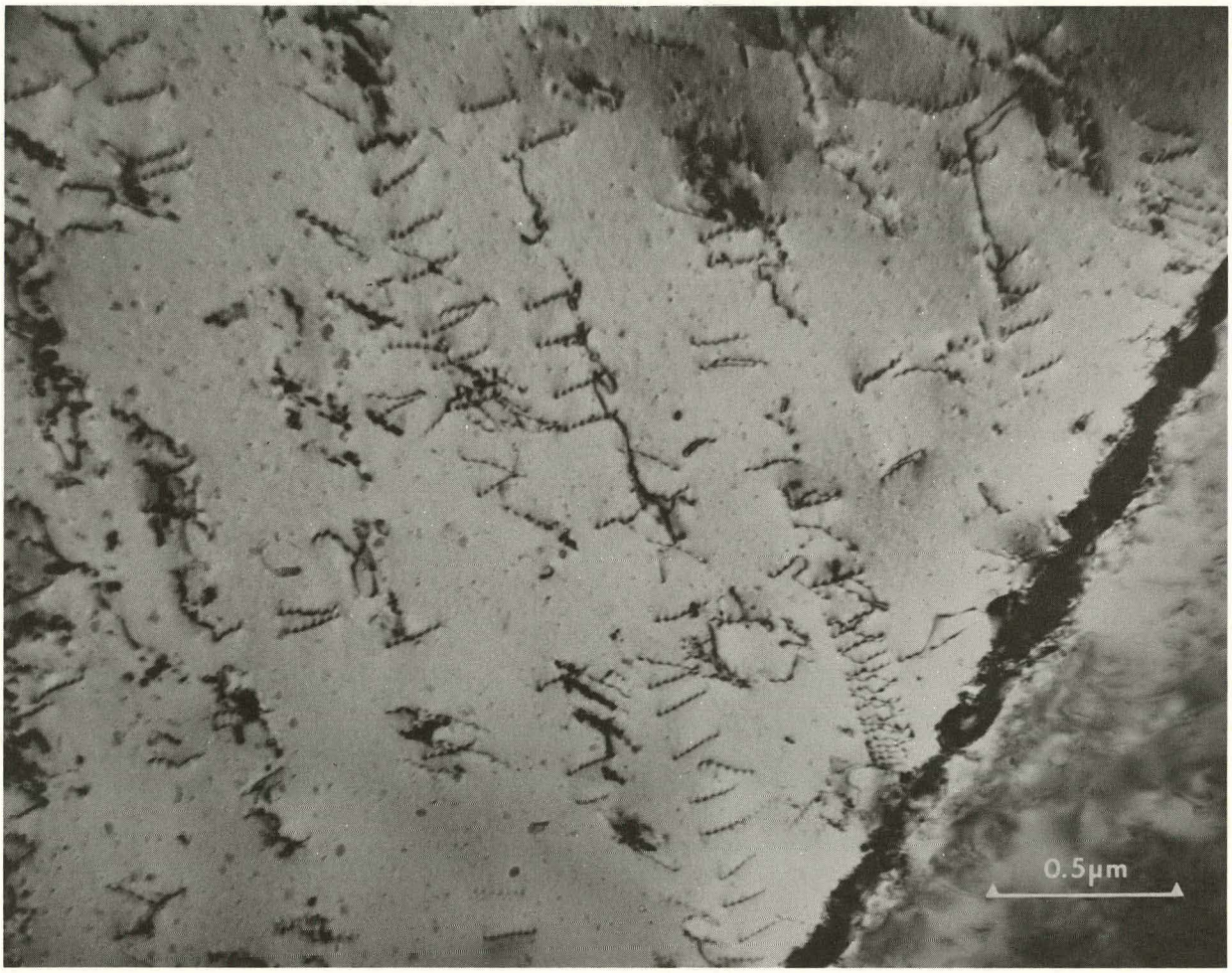

Fig. 2 - Dislocation pile-ups at grain boundary precipitates ($Cr_{23}C_6$) in a specimen that had been aged for 8000 h at 538°C prior to testing at ε_r = 0.6 pct.

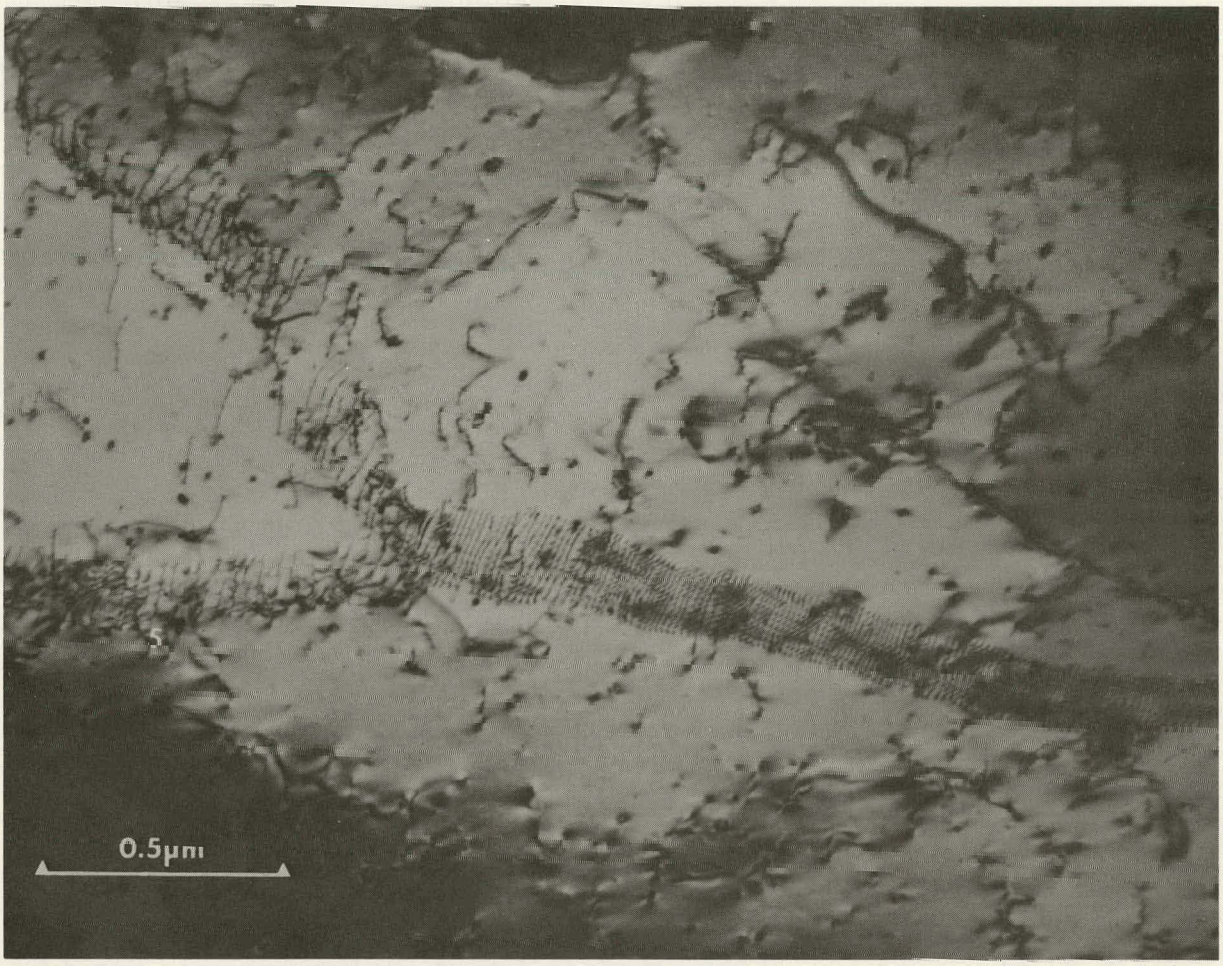

Fig. 3 - Subgrain boundary in a specimen that had been cold worked 10 pct prior to aging 4000 h at 760°C. The specimen was tested at ε_f = 2 pct.

to the deformation axis. Kestenbach further observes that if the stress mode is changed, the sense of the partial separation is reversed with respect to its equilibrium configuration. Thus, a grain that shows no cross slip during the tensile portion of the deformation cycle can show some cross slip during the compression portion and vice versa. This cross-slip mechanism appears to be consistent with the dislocation structure observed in this work.

4.2. Mechanical Behavior

4.2.1. Cyclic Hardening and Softening. Generally, during strain-controlled fatigue testing, a material will experience an initial period of either hardening or softening followed by a long period of stable stress-strain behavior that lasts until failure (Fig. 4). The cyclic hardening and softening behavior of alloy 800H is discussed in this section; the stable stress-strain state, which is commonly called saturation, is discussed in Section 4.2.2.

Table VI shows the cyclic hardening and softening behavior of the specimens tested in this work. The cyclic hardening response, $\Delta\sigma_r$, is defined as the difference between the saturation stress range and the initial stress range. Table VI also gives the number of cycles required to achieve saturation. In certain tests where cyclic softening occurred, the material did not saturate; in these cases the hardening response was calculated by subtracting the first-cycle stress range from the stress range of the last cycle where the stresses were not obviously influenced by cracking. In Table VI an entry proceeded by a minus sign indicates that the material softened. The specimens listed in the table are separated into two categories, aged and non-aged, because the non-aged specimens generally hardened to a higher saturation stress range than the aged specimens. This difference in hardening behavior is thought to be due to differences in dislocation annihilation rates.

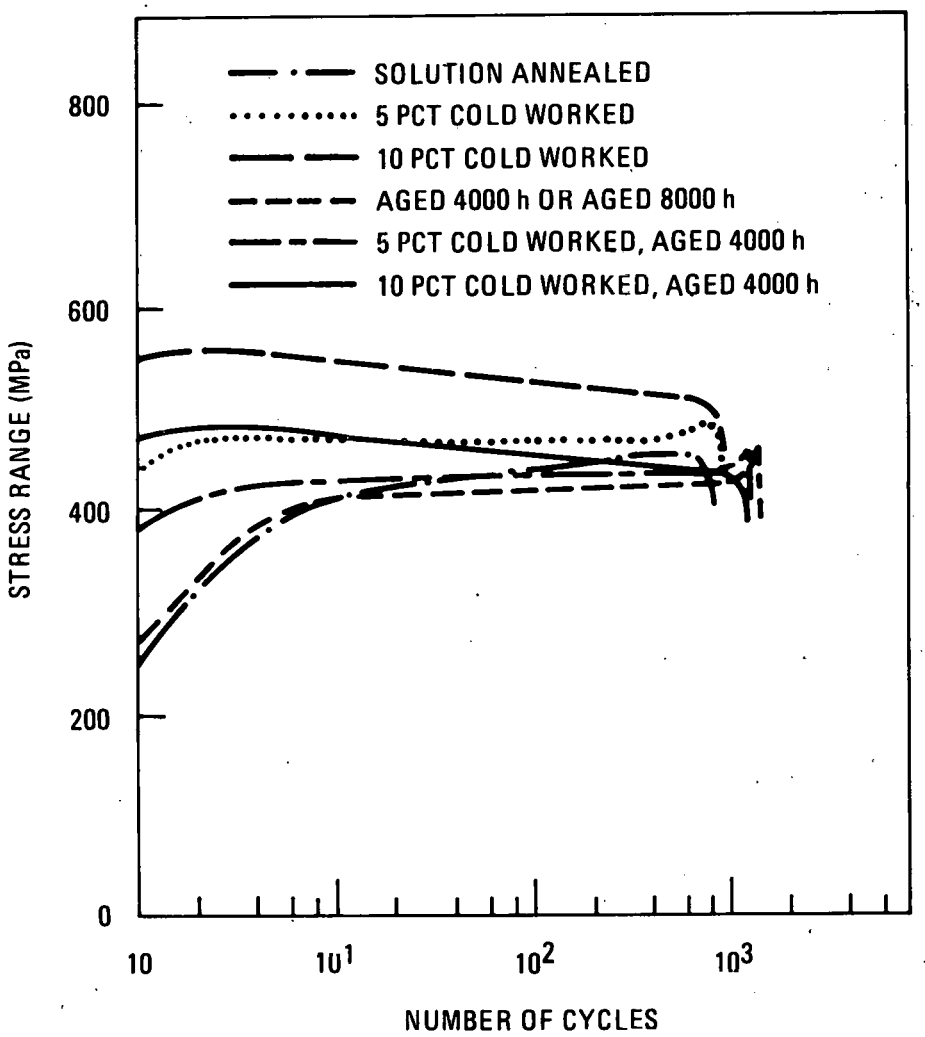

Fig. 4 - The variation of the stress range during testing of specimens at 760°C and ε_r = 1 pct. The two specimens with the highest initial stress ranges softened during testing and did not achieve saturation. All of the other specimens hardened during testing and achieved saturation. Note that the solution-annealed specimen was in saturation for more than one-half of the test.

Table VI. Cyclic Hardening Response and Number of Cycles Required to Achieve Saturation

538°C				593°C				649°C			
Specimen Condition	ε_r, pct	$\Delta\sigma_r$, MPa	Saturation Cycle	Specimen Condition	ε_r, pct	$\Delta\sigma_r$, MPa	Saturation Cycle	Specimen Condition	ε_r, pct	$\Delta\sigma_r$, MPa	Saturation Cycle
Solution annealed	2.0	576	100	Solution annealed	2.0	507	50	Solution annealed	2.0	484	50
	1.5	488	100		1.0	409	200		1.0	403	200
	1.0	417	200		0.75	353	500		0.75	368	1,000
	0.6	398	20,000		0.6	327	5,000		0.6	305	2,000
	0.5	396	5,000		0.5	289	20,000				
								5 pct c.w.	1.0	261	100
5 pct c.w.	1.0	186	200	5 pct c.w.	0.75	175	200		0.6	153	5,000
	0.6	186	20,000		0.5	76	1,000				
								10 pct c.w.	1.0	142	100
10 pct c.w.	1.0	156	200	10 pct c.w.	2.0	304	30		0.6	64	5,000
	0.6	144	20,000		1.0	165	100				
					0.75	106	10,000				
					0.6	107	10,000				
					0.5	116	50,000				
4000 h	2.0	485	50	4000 h	2.0	327	20	4000 h	2.0	169	10
	1.0	255	4,000		1.0	116	20		1.0	87	20
	0.75	222	10,000		0.75	33	10		0.75	92	50
	0.6	202	20,000		0.6	1	10		0.6	90	50
8000 h	2.0	405	50	5 pct c.w.;	1.0	-111	500	5 pct c.w.;	1.0	71	10
	1.0	255	500	4000 h	0.6	-106	10,000	4000 h	0.6	13	50
	0.75	237	7,000								
	0.6	193	20,000								
				10 pct c.w.;	2.0	-84	DNS*	8000 h	2.0	134	10
5 pct c.w.,	1.0	18	10	4000 h	1.0	-155	DNS		1.0	80	20
4000 h	0.6	26	10		0.75	-157	DNS		0.75	87	50
					0.6	-114	DNS		0.6	41	50
10 pct c.w.;	1.0	-49	DNS					10 pct c.w.;	1.0	9	10
4000 h	0.6	-76	30,000					4000 h	0.6	-27	DNS

Table VI. Continued

704°C				760°C			
Specimen Condition	ε_r, pct	$\Delta\sigma_r$, MPa	Saturation Cycle	Specimen Condition	ε_r, pct	$\Delta\sigma_r$, MPa	Saturation Cycle
Solution annealed	2.0	293	20	Solution annealed	2.0	232	10
	1.0	281	20		1.0	198	20
	0.6	140	100		0.5	146	50
	0.5	158	200		0.4	130	500
					0.3	90	1,000
5 pct c.w.	1.0	100	20				
	0.6	63	200	5 pct c.w.	1.0	34	10
					0.6	-63	1,000
10 pct c.w.	1.0	41	10				
	0.6	25	10	10 pct c.w.	2.0	2	10
					1.0	-38	DNS
					0.6	-58	DNS
					0.5	-30	DNS
4000 h	2.0	196	10	4000 h	2.0	179	10
	1.0	157	50		1.0	149	20
	0.6	125	100		0.6	96	50
					0.5	104	50
5 pct c.w.;	1.0	83	10				
4000 h	0.6	38	10	8000 h	2.0	152	10
					1.0	155	10
					0.6	47	10
10 pct c.w.;	1.0	-28	DNS		0.5	109	50
4000 h	0.6	-38	DNS				
				5 pct c.w.;	1.0	40	10
				4000 h	0.6	-10	1,000
				10 pct c.w.;	2.0	-4	DNS
				4000 h	1.0	-37	DNS
					0.6	-75	DNS
					0.5	-69	DNS

*DNS = did not saturate.

Certain trends in Table VI can be identified. First, increasing the cyclic strain range, ε_r, results in an increased $\Delta\sigma_r$ as well as faster saturation. This observation also holds true for the softeners. Indeed, in several cases softening occurred at low values of ε_r while hardening occurred at the highest value of ε_r. The softeners all had prior deformation, and usually they did not reach saturation. Second, as the yield strength increases, the hardening response decreases. One reason for this is that at a constant ε_r, raising the yield strength results in a decreased plastic strain. Another reason is that the cold-working treatments result in an increased Bauschinger effect upon reverse loading. It is also interesting that trends involving the yield strength are not so apparent when both the aged and non-aged data are mixed.

There are some interesting thermal trends that can be identified in Table VI. For instance, $\Delta\sigma_r$ decreases with increasing temperature while the saturation rate increases. This is felt to be partly due to the usual thermal processes involving dislocations, as well as dynamic strain aging. (Dynamic strain aging is discussed in more detail in Section 4.2.2.) Generally, the decrease in $\Delta\sigma_r$ with temperature proceeds in an orderly fashion, but for the aged specimens at 649°C it takes a surprisingly large drop. These specimens showed γ' formation and also a damping of the serrated yielding (see Part I). Perhaps carbon, which is shown in Section 4.2.2 to be responsible for the dynamic strain aging, is elastically attracted to the γ' nuclei and forms clouds around them. This speculation would be consistent with the γ' composition, $Ni_3(Al,Ti)C_x$, that was reported in Part I. Once carbon is tied up by the γ' nuclei, the dynamic strain aging component to hardening would be reduced, resulting in a diminished $\Delta\sigma_r$.

Table VI also shows that before a specimen cyclically softens, it must have had prior deformation, and in some cases specimens with the appropriate history transformed from hardeners to softeners as ε_r was reduced. Because of the difficulties involved in using dislocations to

model such behavior in a polycrystalline specimen, a heuristic approach, based on the Bauschinger effect, will be used to describe the cyclic softening observed in this work.

Consider a material, such as alloy 800H, that has the same stress-strain curve in both tension and compression. Figure 5 shows the first cycle of a LCF test of this material. (In order to facilitate this discussion, the compression curve is plotted opposite to the way it is recorded.) During the initial tensile loading of the specimen, an energy of deformation, E_T, is imparted to the specimen. Upon reverse loading some of this energy, E_B, is released, resulting in a savings in the total energy of deformation necessary to obtain a certain cumulative strain (namely, 1.5 ε_r) compared to that necessary to obtain the same strain by purely tensile loading. The energy E_B is obtained from three sources. First, because the specimens are polycrystalline, a major contribution is due to long-range stresses that arise upon unloading because of the dissimilar plastic tensile deformation experienced by grains with different orientations. Second, a contribution due to dislocation annihilation occurs when the specimen is reverse loaded. This process is felt to be most important in the aged specimens where grain boundary precipitation of $Cr_{23}C_6$ causes long-range pile-ups of dislocations (Fig. 2). Third, a contribution arises from the interaction between mobile dislocations and matrix obstacles such as forest dislocations and precipitates.

Assuming that ε_r always lies within the range of uniform plastic deformation, the plastic portion of both the tensile and compressive curves can be described by the simple relation $\sigma = K\varepsilon^n$, where K is the strength coefficient and n is the strain hardening exponent. The effect of this energy release during reverse loading is to lower the strain-hardening exponent. It is the magnitude of n that controls the cyclic hardening or softening response. For instance, a specimen will harden if $\sigma_T < \sigma_C$ (Fig. 5). This hardening continues, in decreasing increments, until saturation is reached. At saturation, $\sigma_T = \sigma_C$.

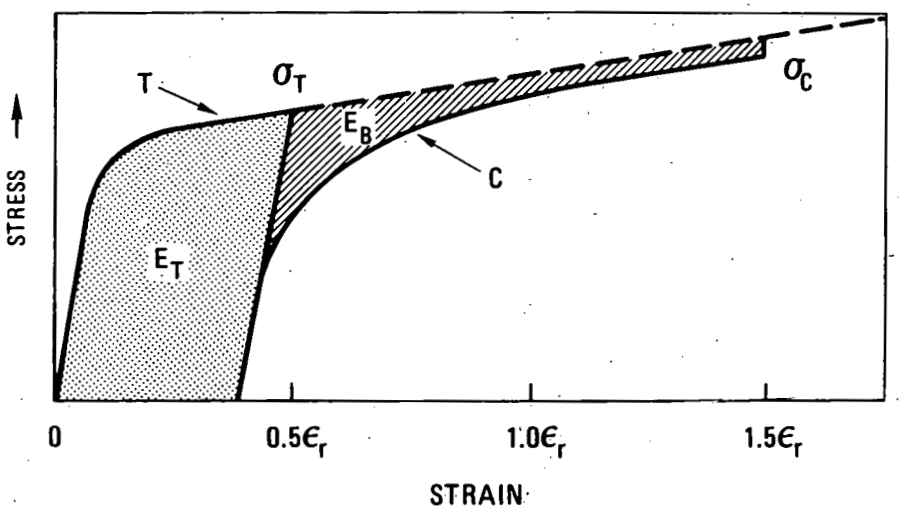

Fig. 5 - Initial stress-strain curves observed during cyclic loading. The curve marked T is the initial tensile curve, and the curve marked C is the initial compression curve plotted opposite to the direction it is recorded. In this example $\sigma_C > \sigma_T$ so that the specimen will cyclically harden.

In order for cyclic softening to occur, the specimen must have had some prior deformation. Figure 6 demonstrates why this is so. Here prior deformation ensures that sufficient energy will be released to cause a decrease in n so that a condition of cyclic softening ($\sigma_T > \sigma_C$) occurs. If the prior deformation is sufficient, it will dominate E_T so that increasing ε_r will have little effect on the compression curve. Consequently, it is possible, even with prior deformation, that the specimen will harden at some increased value of ε_r. It is also possible that a material with prior deformation will show no hardening or softening response if ε_r is selected such that $\sigma_T = \sigma_C$.

4.2.2. Saturation. The cyclic stress-strain curve is a convenient way to describe the saturation stress-strain state of a material. This curve is obtained by plotting the saturation stress range against the plastic strain range. The cyclic stress-strain data for the specimens that saturated are shown in Fig. 7. It is apparent in this figure that the saturation stresses, at a given plastic strain range, depend upon the initial condition of the material. Consequently, the saturation flow stresses in alloy 800H are history dependent.

The dominant feature of this history dependence is that the saturation stresses of the aged specimens fall below those of the specimens that have not been aged. This is thought to be a reflection of the importance of dislocation annihilation processes that occur in the aged specimens upon reverse loading. Because of these annihilation processes, the aged specimens showed less dislocation debris and lower dislocation densities than the non-aged specimens; these differences are thought to explain the observed differences in saturation stresses.

Cyclic stress-strain curves are generally shaped like flow curves; the upward curvature in the 538°C data (Fig. 7a) and the linearity of the 593°C data (Fig. 7b) are thus unusual. Behavior similar to that shown in Figs. 7a and 7b was reported in Ref. 5, where the authors favored an explanation of this effect based on the formation of γ'. However, the

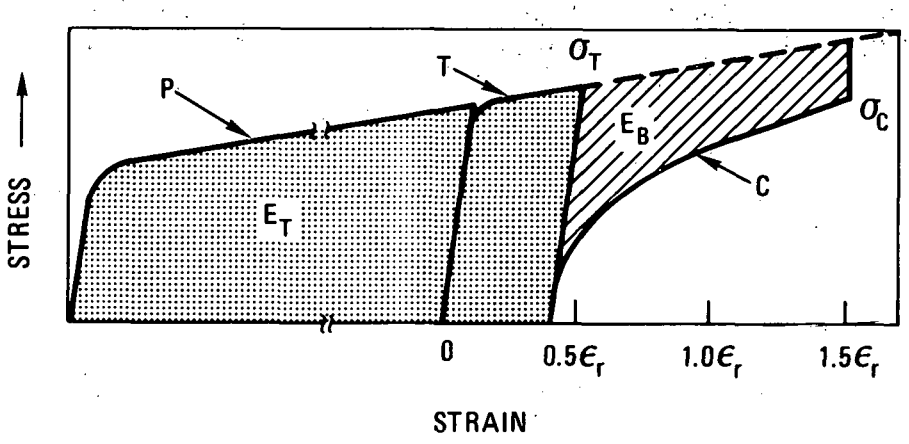

Fig. 6 - Initial stress-strain curves observed in a specimen having prior deformation. The stress-strain curve during the prior deformation is marked P, the initial cyclic tensile deformation curve is marked T, and the compression curve is marked C. Because of the prior deformation, the released energy, E_B, is large and $\sigma_C < \sigma_T$ so that cyclic softening occurs.

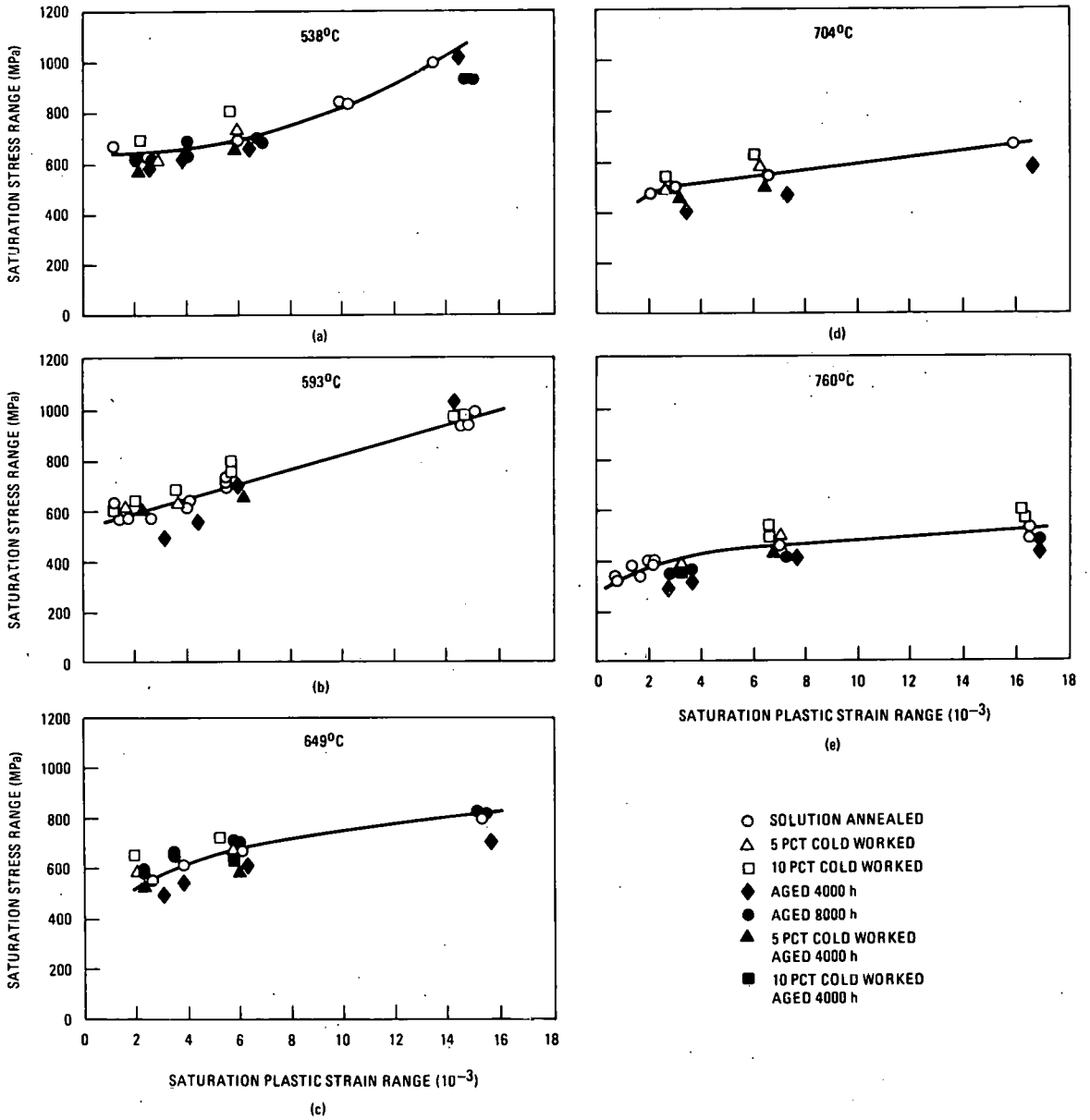

Fig. 7 - Cyclic stress-strain data for specimens that attained saturation. Curves have been drawn through the solution-annealed data.

experiments described in Section 4.1 rule out the possibility that the cyclic stress-strain behavior of alloy 800H at 538°C might be affected by the precipitation of new phases. For example, γ' was not observed in any of the LCF specimens tested at 538°C. Also, only small amounts of $Cr_{23}C_6$ and Ti(C,N) formed at 538°C during testing.

The hardening mechanism that is responsible for the unusual shape of the 538 and 593°C cyclic stress-strain curves is dependent on both temperature and plastic strain range. This is shown in Fig. 8, where the saturation stress range is plotted versus testing temperature for two different plastic strain ranges. The region S in this figure shows the temperature range over which serrated yielding occurred; the peaks in the curves coincide with this region. These observations argue that dynamic strain aging occurs in the temperature range ~450 to 650°C and is maximized at ~550°C.

It is possible to make an educated guess about the identity of the atomic species that is responsible for the dynamic strain aging. Figure 8 indicates that the hardening is maximized at 550°C, so that at this temperature the velocity of the solute species responsible for the dynamic strain aging is approximately equal to the velocity of the mobile dislocations. Now assume the average dislocation velocity is given by $V_d = \dot{\varepsilon}/\rho b$, where ρ is the dislocation density, b is the magnitude of the Burgers vector, and $\dot{\varepsilon}$ is the strain rate. Taking $\rho = 10^8$ cm^{-2} and $b = 3 \times 10^{-8}$ cm gives $V_d \simeq 10^{-3}$ cm/s. The maximum velocity at which an edge dislocation can drag a Maxwellian atmosphere along is given by $V_a = 4D/L$, where D is the diffusivity of the solute atom and L is the radius of the atmosphere. For substitutional elements, such as Ti and Al, $D \simeq 4 \times 10^{-17}$ cm^2/s at 550°C and $L \simeq 10b$. These values yield $V_a \simeq 10^{-8}$ cm/s, a velocity that does not correspond well with the estimated dislocation velocity. A much more reasonable candidate would be an interstitial element such as carbon. For instance, at 550°C the diffusivity of carbon in austenite is $D \simeq 2 \times 10^{-11}$ cm^2/s; assuming $L \simeq 30b$, then $V_a \simeq 10^{-4}$ cm/s. Since

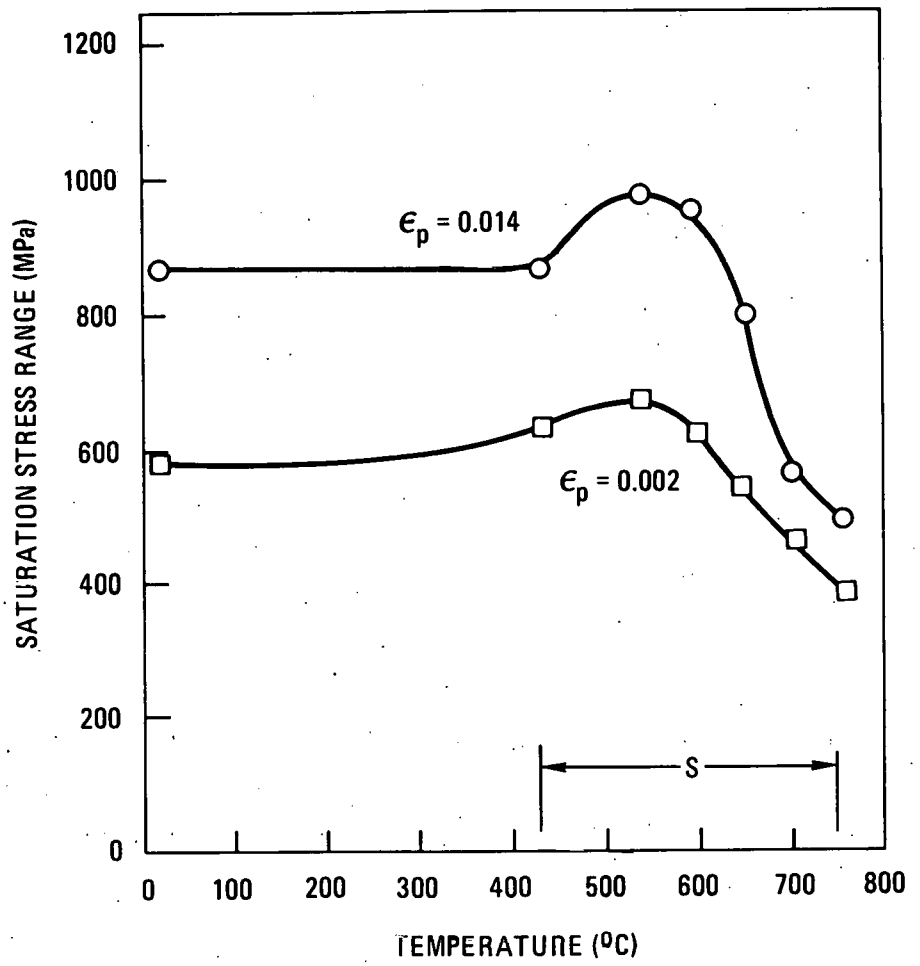

Fig. 8 - Saturation stress range of solution-annealed specimens as a function of the testing temperature. The data points at 20 and 430°C were obtained in a series of tests not discussed in this paper. Serrated yielding was observed in specimens that were tested in the temperature range S.

interstitials may form a condensed atmosphere, this value of V_a is only a lower limit, and thus the correspondence with V_d is fairly good. Finally, an argument favoring carbon as the interstitial element responsible for the dynamic strain aging is that most of the nitrogen is tied up as TiN during the manufacture of the alloy, while only about one-half of the available carbon is ever used in forming $Cr_{23}C_6$.

4.2.3. Failure. Fatigue crack initiation was studied by means of interrupted tests in which the specimen was removed from the testing machine and the surface examined using a scanning electron microscope. After the examination, the specimen was reinserted into the testing machine, and the test continued until the next interruption. Using this protocol, the first small cracks were detected at about 10% of the number of cycles required to produce macroscopic failure of the specimen.

The fatigue cracks initiated at the intersection of slip bands with the specimen surface (Fig. 9). As cyclic loading continued, both the average crack length and the number density of cracks increased. In specimens tested at the higher strain ranges, where the crack density was relatively high, small parallel cracks often formed on adjacent slip bands and then coalesced into one main crack giving a zipper pattern to the crack, as shown in Fig. 10. This crack coalescence may occur simultaneously with the transition from stage I propagation along the slip bands to stage II propagation perpendicular to the specimen axis.

The fracture path was transgranular under all of the conditions used in this study, and as the crack moved across the specimen it left fatigue striations in its wake. Metallographic analysis of the fracture surface showed no evidence to link TiN, the large matrix particles that are found in every few grains, with either fracture initiation or propagation. However, the presence of an oxide layer on the fracture surface suggested that the environment likely influenced the propagation mechanism, and indeed for a few specimens tested in vacuum, the fatigue life was about an order of magnitude greater than that of specimens tested in air.

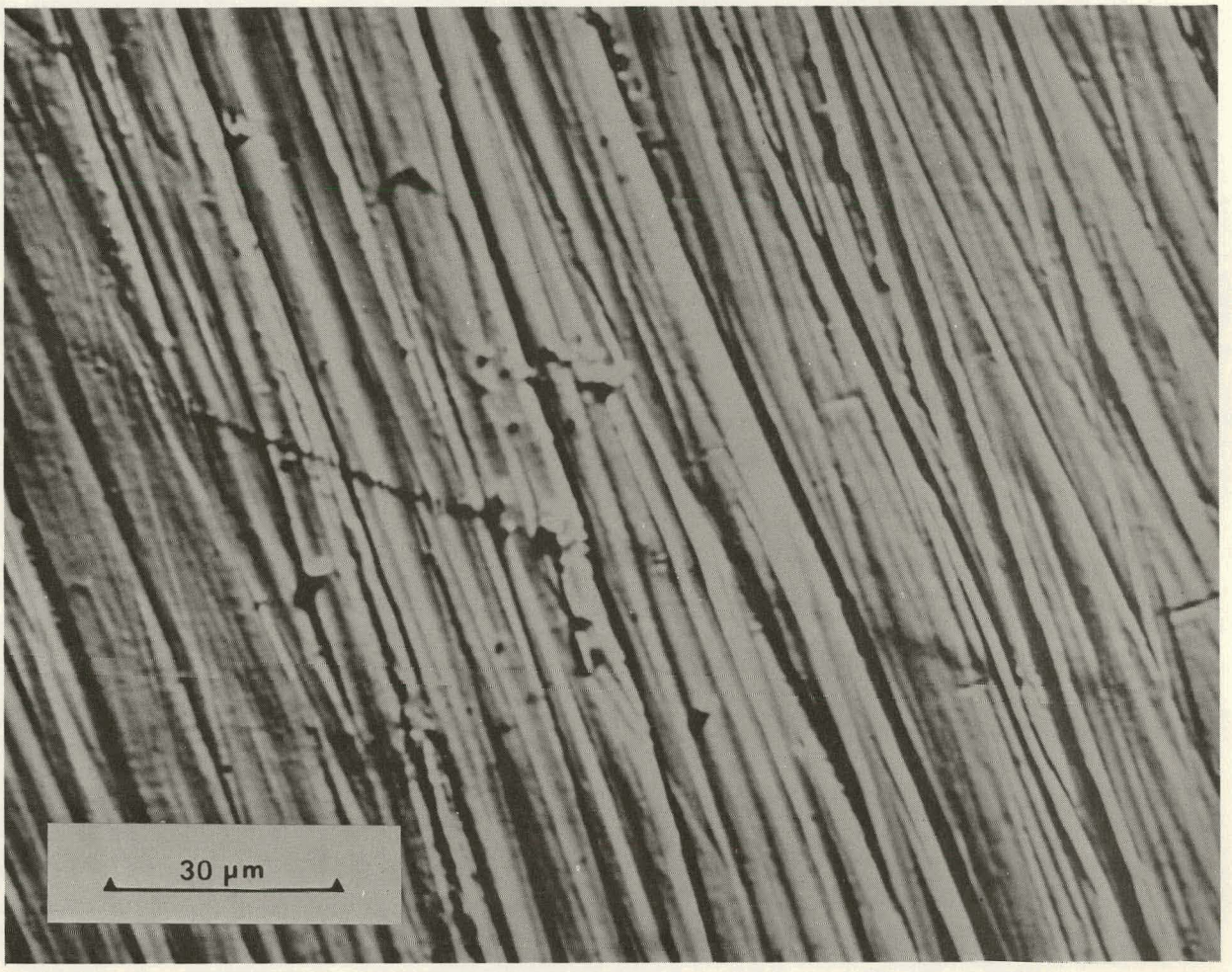

Fig. 9 - Back-scattered image of a small crack initiating on the surface of a solution-annealed specimen after 20 deformation cycles. The specimen was tested at 649°C with ε_r = 2 pct. The scratches are normal polishing marks, parallel to the axis of the specimen.

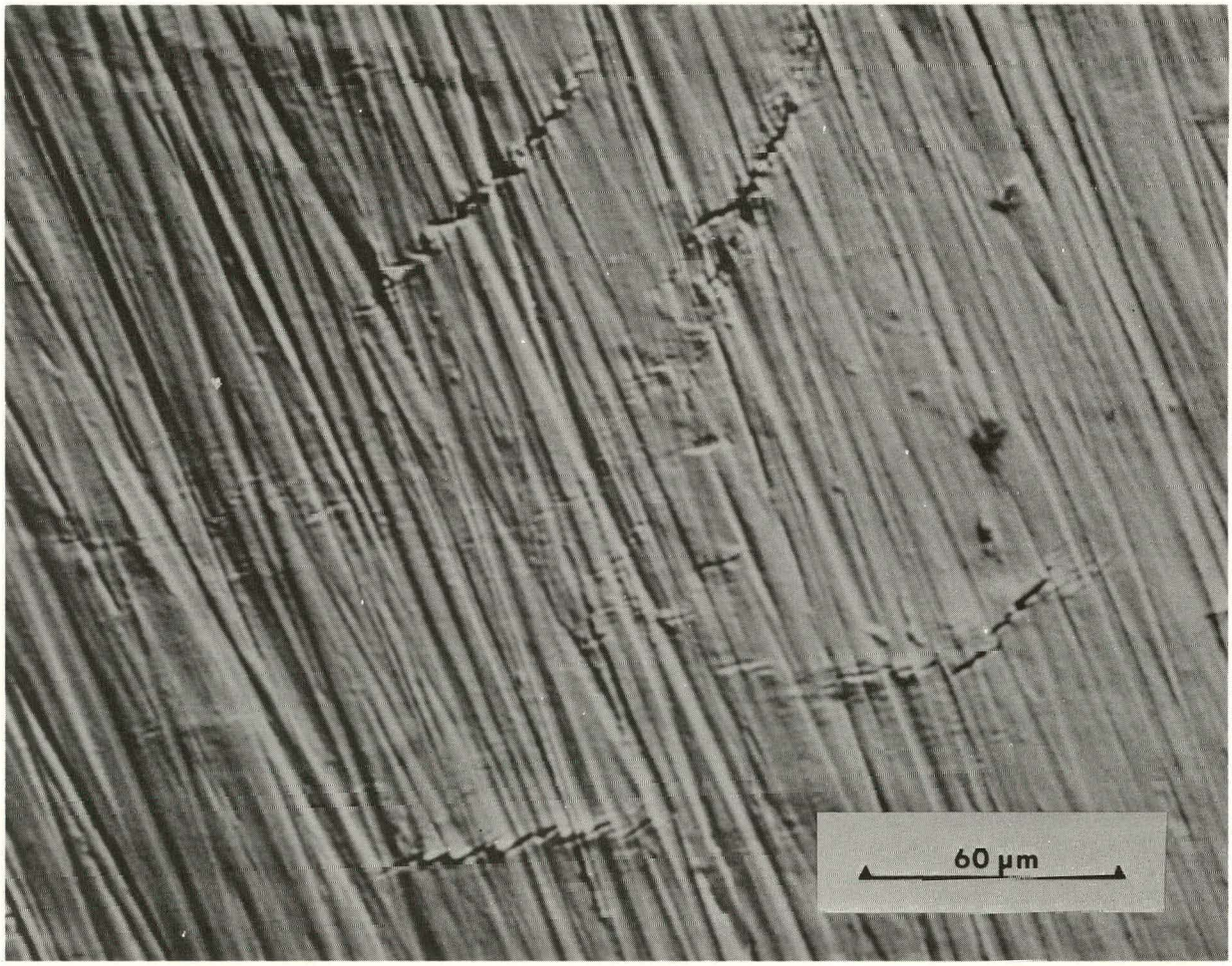

Fig. 10 - Back-scattered image of the same specimen shown in Fig. 9 after 50 cycles. The zipper-shaped cracks are caused by the coalescence of a number of small parallel cracks formed on adjacent slip bands.

Macroscopic failure was indicated by a rapid decrease in the stress range experienced by the specimen, as distinguished from the slow decrease in the stress range observed in specimens that cyclically softened. The fatigue life associated with macroscopic failure was defined as the point where there was a 5% difference between the stress range extrapolated from earlier behavior and the actual stress range. Figure 11 shows curves of strain range versus life; there is some evidence of a weak trend in these data indicating that the aged specimens have the longest life. This is expected because the saturation stress is history dependent. In order to see this, consider the following argument.

Tompkins[6] has developed a fatigue-crack propagation model that predicts the following relationship between fatigue life and plastic strain range: $N_f = (c/k^2)\ \varepsilon_p^{-1/(2\beta + 1)}$, where c, k, and β are constants. (This equation is functionally similar to the empirically observed Coffin-Manson equation.) The constants k and β appear in an expression describing the cyclic stress-strain curve: $\sigma_r = k\varepsilon_p^{\beta}$. Thus, Tompkin's model predicts that the fatigue life will be history dependent if the cyclic stress-strain curve is history dependent. Figure 12 shows Coffin-Manson plots for 538, 649, and 760°C. This figure clearly shows a difference in life between the aged and the non-aged specimens.

The network of grain boundary carbides could influence fatigue crack propagation in two ways. First, back stresses due to pile-ups of dislocations at a grain boundary could restrict the size of the plastic zone at the crack tip as it approaches the boundary, thereby reducing the crack propagation rate. Second, the carbide particles could cause blunting when the crack front encounters the particles at the grain boundary. This would cause a delay in propagation while the normal sharpness was again attained. Thus, part or all of the observed increase in fatigue life of the aged specimens could be explained by a physical interaction of the

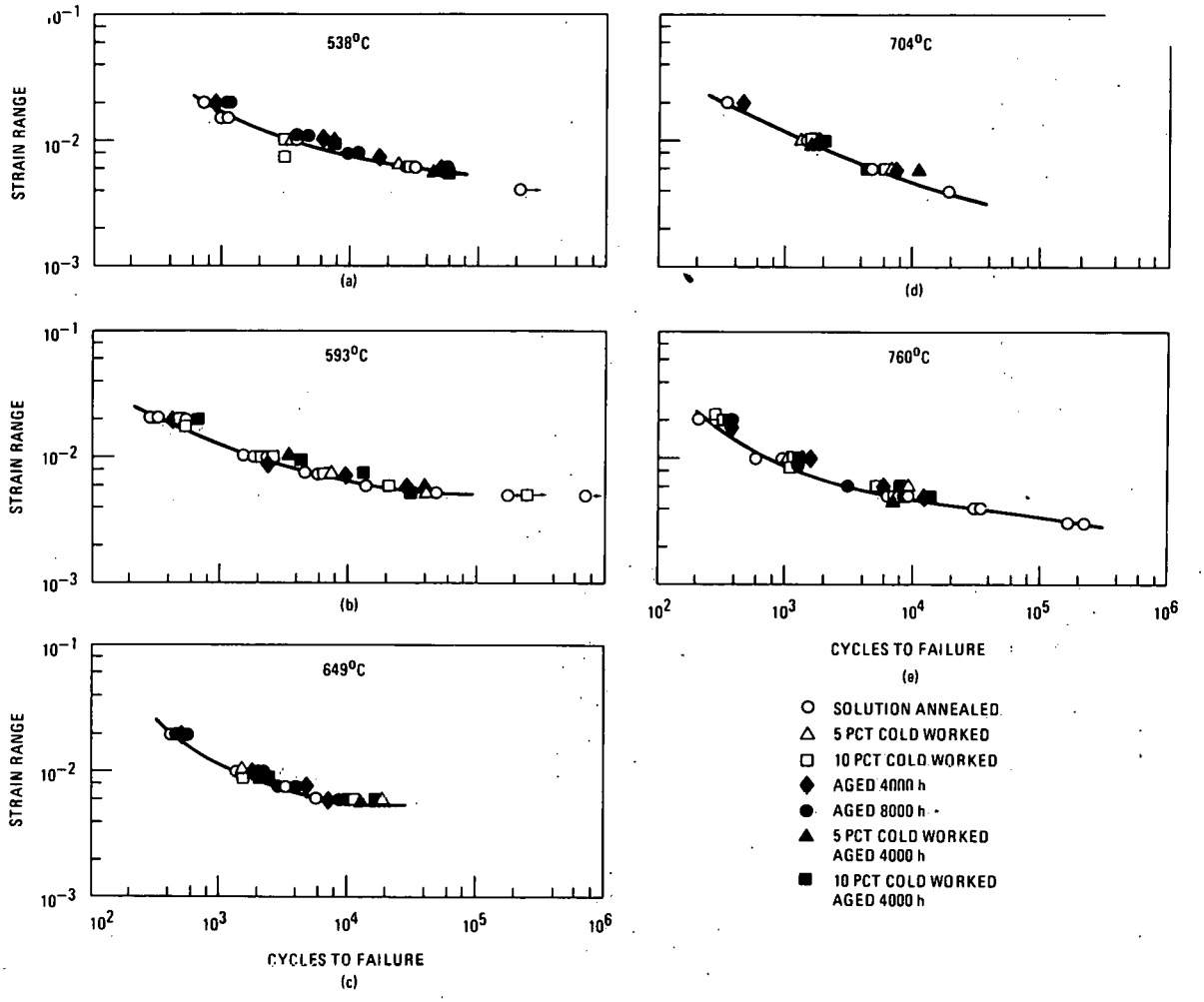

Fig. 11 - Relation between the strain range and the macroscopic fatigue life.

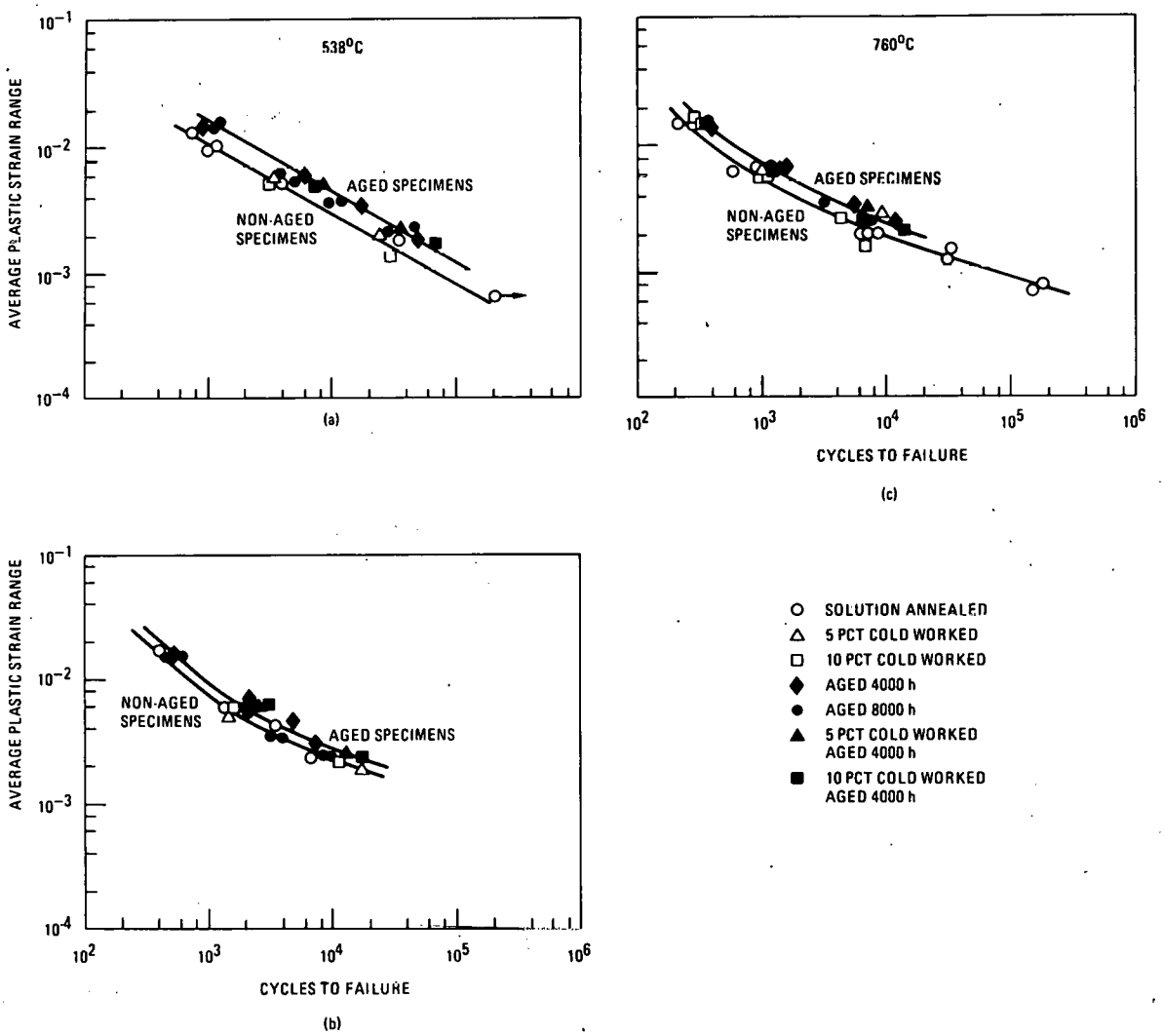

Fig. 12 - Relation between the average plastic strain range and the macroscopic fatigue life. Since the testing time was predominantly spent in the saturation state, the average plastic strain range is essentially the same as the saturation plastic strain range.

crack with the grain boundary particles rather than by differences in the cyclic stress-strain curves.

With the exception of the data obtained at 538°C, the logarithm of the plastic strain range is not linearly related to the logarithm of the fatigue life. Thus, for temperatures above 538°C, alloy 800H does not obey the Coffin-Manson equation. The deviation from linearity occurs for both the aged and non-aged material and, therefore, it is not likely to be related to the state of the $Cr_{23}C_6$ precipitates in the grain boundaries. One possible cause of the nonlinear behavior is the climb of dislocations to form subgrain boundaries. The rearrangement of dislocations to form subgrain boundaries occurs increasingly with testing temperature and time. The subgrain boundary formation that occurs during testing acts to reduce the flow stresses because it produces a lower energy configuration for dislocations. These increasingly lower stresses, with increasing test time, tend to extend the life of the specimen and could produce the observed deviation from linearity.

V. CONCLUDING REMARKS

An important feature of the LCF behavior of alloy 800H is its history dependence. However, it also has a hardening component, dynamic strain aging due to carbon, that is history independent. At temperatures above 538°C the Coffin-Manson plots indicate the existence of a history-independent softening process that increases as the strain range of the test decreases.

The history dependence was identified in the cyclic stress-strain curves. This dependence manifests itself as differences in the saturation stress and the fatigue life. Within the scatter of the experimental data, two obvious trends could usually be identified, one associated with the aged specimens and one with the non-aged specimens. The aged specimens were particularly interesting because of the speculation that exists as

to whether or not γ' precipitation is responsible for mechanical property changes that occur with aging. This work demonstrates that the precipitation of $Cr_{23}C_6$ at grain boundaries is far more important in determining LCF properties than γ'.

ACKNOWLEDGMENTS

The authors wish to thank Dr. P. K. Gantzel and Messrs. C. J. Neff, Jr., and D. R. Wall for laboratory assistance. The useful comments of Drs. C. C. Li and L. D. Thompson are also acknowledged.

REFERENCES

1. R. E. Villagrana, J. L. Kaae, J. R. Ellis, and P. K. Gantzel: Met. Trans., 1978, vol. 9A, p. 927.
2. J. Orr: Proceedings of the Petten International Conference on Alloy 800, W. Betteridge, R. Krefeld, H. Krockel, S. J. Lloyd, M. Van De Voorde, and C. Vivante, eds., North-Holland Publishing Co., 1978, p. 25.
3. L. D. Thompson: private communication.
4. H. J. Kestenbach: Phil. Mag., 1977, vol. 36, p. 1509.
5. H. Nahm and J. Moteff: Met. Trans., 1976, vol. 7A, p. 1473.
6. B. Tomkins: Phil. Mag., 1968, vol. 18, p. 1041.

GENERAL ATOMIC COMPANY
P. O. BOX 81608
SAN DIEGO, CALIFORNIA 92138